Neusser, G., Eppler, S., Bowen, J. , Allender, C. J., Walther, P., Mizaikoff, B. and Kranz, C. 2017. FIB and MIP: understanding nanoscale porosity in molecularly imprinted polymers via 3D FIB/SEM tomography. Nanoscale 9 (38) , pp. 14327-14334. 10.1039/C7NR05725C

Publishers page: http://dx.doi.org/10.1039/C7NR05725C

Nanoscale

This article can be cited before page numbers have been issued, to do this please use: G. Neusser, S. Eppler, J. L. Bowen, C. J. Allender, P. Walther, B. Mizaikoff and C. Kranz, *Nanoscale*, 2017, DOI: 10.1039/C7NR05725C.

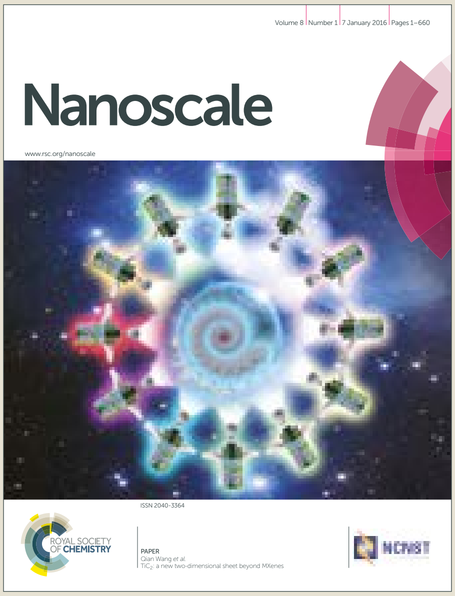

Volume 8 | Number 1 | 7 January 2016 | Pages 1–660

Nanoscale

www.rsc.org/nanoscale

ISSN 2040-3364

ROYAL SOCIETY OF CHEMISTRY

PAPER
Qian Wang *et al.*
TiC_2: a new two-dimensional sheet beyond MXenes

ROYAL SOCIETY OF CHEMISTRY

rsc.li/nanoscale

View Article Online
DOI: 10.1039/C7NR05725C

Journal Name

ARTICLE

FIB and MIP: Understanding Nanoscale Porosity in Molecularly Imprinted Polymers via 3D FIB/SEM Tomography

Received 00th January 20xx,
Accepted 00th January 20xx

DOI: 10.1039/x0xx00000x

www.rsc.org/

G. Neusser,[a] S. Eppler,[a,d] J. Bowen, [b] C. J. Allender, [b] P. Walther, [c] B. Mizaikoff, [a*] and C. Kranz [a*]

We present combined focused ion beam/scanning electron beam (FIB/SEM) tomography as innovative method for differentiating and visualizing the distribution and connectivity of pores within molecularly imprinted polymers (MIPs) and non-imprinted control polymers (NIPs). FIB/SEM tomography is used in cell biology for elucidating three-dimensional structures such as organelles, but has not yet been extensively applied for visualizing the heterogeneity of nanoscopic pore networks, interconnectivity, and tortuosity in polymers. To our best knowledge, the present study is the first application of this strategy for analyzing the nanoscale porosity of MIPs. MIPs imprinted for propranolol - and the corresponding NIPs - were investigated establishing FIB/SEM tomography as a viable future strategy complementing conventional isotherm studies. For visualizing and understanding the properties of pore networks in detail, polymer particles were stained with osmium tetroxide (OsO_4) vapor, and embedded in epoxy resin. Staining with OsO_4 provides excellent contrast during high-resolution SEM imaging. After optimizing the threshold to discriminate between the stained polymer matrix, and pores filled with epoxy resin, a 3D model of the sampled volume may be established for deriving not only the pore volume and pore surface area, but also to visualize the interconnectivity and tortuosity of the pores within the sampled polymer volume. Detailed studies using different types of cross-linkers and the effect of hydrolysis on the resulting polymer properties have been investigated. In comparison of MIP and NIP, it could be unambiguously shown that the interconnectivity of the visualized pores in MIPs is significantly higher vs. the non-imprinted polymer, and that the pore volume and pore area is 34 % and approx. 35% higher within the MIP matrix. This confirms that the templating process not only induces selective binding sites, but indeed also affects the physical properties of such polymers down to the nanoscale, and that additional chemical modification, e.g., via hydrolysis clearly affects that nature of the polymer.

Introduction

3D structural information at the micro- and nanoscale of any material including electrodes in fuel cells and batteries,[1,2] adsorption materials for chromatography,[3] and functional polymers[4] is a key prerequisite for understanding their chemical, physical, and physico-chemical behavior. Among functionalized polymers, molecularly imprinted polymers (MIPs) have gained significant interest as tailorable, selective, and synthetic receptor materials based on highly cross-linked polymeric networks with applications as biomimetic recognition elements in chem/biosensors and pseudo-immunoassays,[5,6] as synthetic carrier material in drug delivery,[7] or as stationary phase in liquid chromatography and in solid phase extraction[8,9]. The synthesis of MIPs comprises the co-polymerization of suitable functional monomers in the presence of a target molecule (i.e., template) with a cross-linker, thereby ‘imprinting’ the functionality – and to a lesser extent the size and shape - of the template into binding sites of the generated 3D polymer architecture.[10,11] Due to the presence of the template during polymerization, it is expected that selective binding sites are obtained and the porosity of the material is likely to be altered after removal (i.e. extraction) of the usually low molecular weight template molecules. Besides the influence of the template removal step, we intentionally performed partial hydrolysis of the cross-linked polymer matrix for increasing the efficiency of template removal, and to improve accessibility of the resultant binding sites in the shown example here. This was achieved by preparing MIPs using two different cross-linking monomers. The criteria for selecting these monomers was that after the polymerization cross-links arising from one monomer could be selectively cleaved in the presence of a second monomer. The two monomers selected were divinylbenzene (DVB) and ethylene glycol dimethacrylate (EGMA) (see Table S1), since the ester cross-link resulting from the polymerization of EGMA could readily be hydrolyzed at conditions that would not affect the DVB cross-link. Polymer macroporosity is an important factor influencing in defining both binding capacity and kinetics.[12] MIP performance is therefore not only dependent on the properties of the binding sites, but also on their accessibility, which is largely determined by the nature of the pore network including its interconnectivity, pore size distribution, and tortuosity. Hence, these parameters are relevant for tailoring and deliberately controlling the performance characteristics of MIPs. Typically, MIPs are described by their binding capacity, binding selectivity and imprinting efficiency, which are bulk parameters and do not provide any structural information

---

[a] *Institute of Analytical and Bioanalytical Chemistry, Ulm University, Albert-Einstein-Allee 11 89081 Ulm, Germany. E-mail: christine.kranz@uni-ulm.de,*
[b] *Cardiff School of Pharmacy and Pharmaceutical Sciences, Cardiff University*
[c] *Central Facility for Electron Microscopy, Ulm University, Albert-Einstein-Allee 11 89081 Ulm, Germany.*
[d] *Cotton Mouton Diagnostics Ltd., Cardiff*

View Article Online
DOI: 10.1039/C7NR05725C

on the actual polymer matrix. The efficacy of a MIP is frequently reported in terms of its ability to selectively bind its template beyond that of a control polymer, i.e., a non-imprinted polymer (NIP), which is synthesized at the same conditions as the MIP, but in absence of a template. While it is usually anticipated that both, MIP and NIP exhibit similar physical properties as documented in a wealth of literature on synthesis and application of MIPs, only few studies are concerned with a detailed characterization of the pore network and pore connectivity within these materials, and how much MIP and NIP are indeed alike.[13,14] Even after exhaustive extraction, template molecules may be retained within the polymer matrix,[12] which indicates that either template molecules may be completely embedded into the polymer matrix or that the pores are not sufficiently interconnected for facilitating complete extraction.

In general, pores are classified as macropores (diam. >50 nm), mesopores (diam. 2–50 nm), and micropores (diam. <2 nm). Conventionally, polymer porosity and structure is investigated using methods such as gas-phase adsorption isotherms (e.g., nitrogen) such as Brunauer-Emmett-Teller (BET) isotherms,[15] Barrett-Joyner-Halenda (BJH) isotherms,[16] and mercury porosimetry,[17] are recorded for deriving structural information including surface area and pore size distribution in MIP/NIP material.[18] While these methods have proven extremely useful in exploring polymer structure, they are fundamentally indirect approaches with data susceptible to over analysis and artifactual outcomes. Transmission electron microscopy (TEM) and high-resolution SEM are frequently applied for characterizing MIPs and NIPs in respect to particle size, size distribution, and for analyzing MIP composite particles (e.g., magnetic MIPs),[19] but so far no detailed structural information on the actual pore structure has been provided by these techniques.

Information on porosity and interconnectivity at the micro- and nanoscale for various materials is accessible via methods such as µ-computer tomography (µCT), x-ray tomography, TEM tomography, and tomography using focused ion beam/scanning electron microscopy (FIB/SEM)[20]. FIB/SEM tomography has gained in popularity and importance on the basis that large sections of a sample may be reconstructed. This is in contrast to techniques such as TEM tomography, where only small sections of a sample can be analyzed.[21] Furthermore, signal absorption is not a limiting factor as compared to x-ray-based techniques.[22] FIB/SEM tomography has become an indispensable tool in many research areas ranging from characterizing ceramics, metals and alloys, rocks and minerals, fuel cell materials, and even biological specimen such as cells. [23-27] State-of-the-art FIB/SEM dual beam instruments facilitate such studies with a spatial resolution down to approx. 1 nm even in materials with low densities containing predominantly elements with low atom numbers including polymers or biological samples. However, appropriate sample preparation strategies are a prerequisite. For biological systems, sample preparation is mainly performed by high-pressure freezing, freeze substitution, and epoxy embedding (e.g., Epon), as described by Walther and Ziegler.[28] To the best of our knowledge, FIB/SEM tomography have to date only be used for characterizing polymer nano-composite materials (i.e., halloysite nanotube (HNT) polypropylene composites),[29] but has not yet been applied to investigate the porosity, interconnectivity, and tortuosity of functional polymers such as MIPs. Even less so for a comparison with their non-imprinted analogues, i.e., NIPs. The enhanced template selectivity of a MIP compared to a NIP is assumed to result from the generation of template-specific binding sites resulting from a templating process entailing capture and removal of a molecular species during pre-polymerization self-assembly, polymerization, and template removal, while largely ignoring potentially significant differences in polymer morphology, i.e., properties of the pore network when comparing MIP with NIP.

In the present study, we focus on this aspect, and introduce FIB/SEM tomography (Fig. 1) as a method for analyzing and comparing the structural properties of a MIP and NIP, which is demonstrated for propranolol-imprinted polymers and their respective NIP controls. Propranolol is a beta-blocker commonly serving as model template in molecular imprinting studies.[30–32]

Results and discussion

During the studies presented herein, eight different polymers (i.e., M0, MH0, N0, NH0 and M40, MH40 and N40, NH40), which composition is provided in Table S1, have been investigated. For all MIPs and NIPs, DVB was used as cross-linker. For M40 and N40, 40% EGDMA was added to the polymerization mixture. MH0, NH0, MH40, NH40 reflect polymers, which were hydrolyzed after the polymerization process. Hydrolysis should effectively induce changes within the EGDMA cross-linker backbone, and increase the accessibility to binding sites.

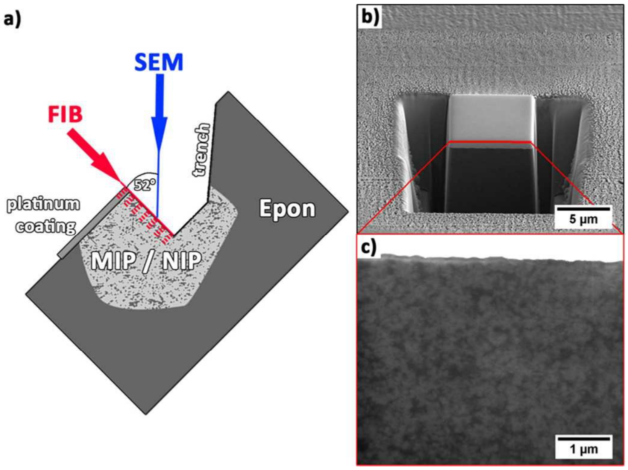

Fig. 1 a) Schematic of the ‘slice-and-view’ procedure in FIB/SEM tomography. After preparation of a trench within a polymer particle, a SEM image of the front of the prepared block is recorded. Then, material at the front is removed by FIB milling again followed by collection of a SEM image. These two steps are then repeated automatically (i.e., slice-and-view). b) SEM image of the trench prior to FIB/SEM

View Article Online
DOI: 10.1039/C7NR05725C

tomography. c) SEM image of the front face of the cross-section revealing the Os-loaded polymer (bright) and Epon-filled pores (dark).

Swelling behavior of MIPs and NIPs

In fluids, MIPs and NIPs may swell differentially depending on the solvent and the composition of the imprinted and non-imprinted polymer.[33-35] Therefore, in a first-step the swelling behavior of these materials was investigated, as a difference in the resulting overall volume of MIP and NIP may also result in variations of the associated pore space. As Epoxy resin is liquid prior to polymerization, MIP0 and NIP0 particles were soaked in liquid resin. Then, the polymer particles were placed on a transparent grid, and classified in size using a light microscope before and after embedding. The analysis of small changes in volume for irregularly shaped polymer particles vs. spherical structures is challenging, and only significant differences (at least approximately 25%) are readily detectable. Although this is only an estimate, two important facts may be derived: (i) the change in volume is moderate for all polymer particles; (ii) there was no detectable difference in swelling behavior of the MIP and corresponding NIP when embedded in Epon epoxy resin.

Contrast and thresholding in FIB/SEM tomography

Staining procedures with osmium tetroxide are frequently used, if SEM contrast of the sample is poor (e.g., polymers, biological samples, etc.). Staining the polymer particles enhances the brightness in SEM images of MIP and NIP due to the osmium modification of the double bonds,[36] which in contrast is not occurring in the epoxy resin (Fig. 1 & Fig. 2 a). Therefore, MIP and NIP polymer matrices may be clearly distinguished from epoxy filling the pore space, although no sharp boundaries are observed (Fig. 2a). The obtained images appear to reveal a smooth transition in grey values in contrast to similarly embedded biological samples.[21] The application of a band pass filter when processing the collected image stacks in post image treatment enhances the contrast and the brightness, and removes shadowing effects appearing during image acquisition (Fig. 2b).

The histograms of the image stacks reveal a unimodal distribution (Fig. 2c); hence, defining a useful threshold value for image segmentation is essential. The brightness of a pixel in the SEM images depends on the amount of Os within the sampled volume, which relates to the amount of stained polymer. The pixel is brightest, if the sampled volume solely consists of stained polymer, and appears increasingly darker if the amount of pore space increases relative to the amount of stained polymer within the same interaction volume of the electron beam. In order to determine a useful threshold value, herein pixels with grey values of zero were defined as pure pore space, and the maximum of the histogram (100%) was defined as pure stained polymer. The threshold was then selected as the grey value corresponding to sampling approx. 50% pore space and 50% stained polymer (Fig. 2c). An example of a correspondingly binarized image after application of the threshold with pores marked in black and stained polymer in white is shown in Fig. 2 d).

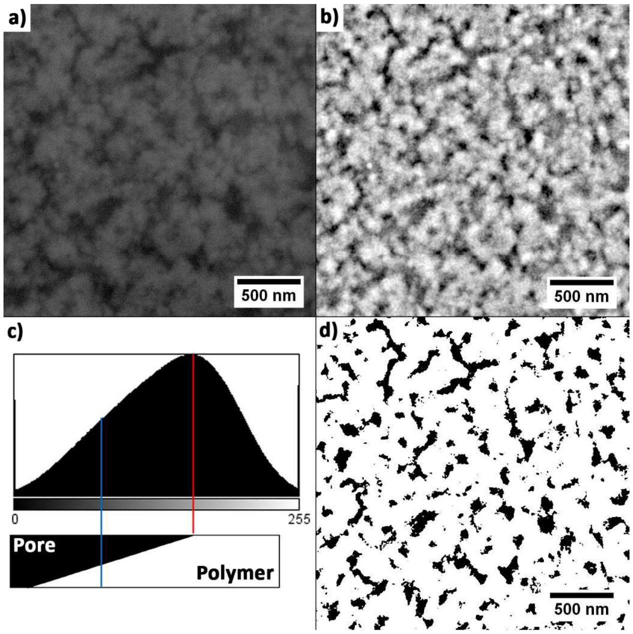

Fig. 2 Image processing of collected SEM image stacks. a) Raw SEM image of MIP0; b) same image after application of a band pass filter; c) histogram of the entire data image stack for MIP0 after application of a band pass filter revealing an almost unimodal distribution of grey values. Peaks at grey value 0 and 255 result from the auto-saturation during application of the band pass filter. The red line indicates the maximum of the histogram. All grey values brighter than the peak value are assumed to represent probed volume consisting only of stained polymer. Darker grey values represent a mixture of stained polymer and epoxy resin. The blue line corresponds to half the grey value of the red line, and therefore indicates 50/50 stained polymer/epoxy resin within the probed volume. This value was used as threshold value. D) Image after binarization with the obtained threshold with the stained polymer matrix now shown in white, and the pore space shown in black.

FIB/SEM tomography procedure

In a next step, 'slice-and-view' was performed within a volume of 2.5 x 2.5 x 0.73 µm at a resolution of 3.57 x 3.57 x 5 nm (i.e., voxel size). The obtained SEM images were then stacked and aligned as described in the experimental section. Typically, MIPs and NIPs are investigated by BET studies, and the relevant parameter describing selective binding is the so-called imprinting factor. However, neither BET data nor the imprinting factor provides information on the porosity and the interconnectivity of pores, which should significantly influence not only the removal of the template molecule, but also the physical and chemical behavior of the polymer. Clearly, specific binding sites, which are in size roughly on the order of magnitude of the template molecules, cannot be resolved with the approach presented here. However, porosity and pore interconnectivity on the order of magnitude of several nanometers can be discriminated, as the resolution of state-of-

View Article Online
DOI: 10.1039/C7NR05725C

the-art FIB/SEM tomography is < 10 nm/pixel[37]. The investigations herein reveal significant differences between MIPs and NIPs, which are summarized in Table 1; the pore size distribution plots are shown in Fig. 3.

	MIP0	NIP0	MIPH0	NIPH0	MIPH40	NIPH40
Total volume [µm^3]	0.74	0.49	0.70	0.48	0.61	0.43
Total surface [µm^2]	138.65	90.63	159.73	96.77	171.84	179.37
Pore space [%]	16.2	10.8	15.4	10.6	13.3	9.5
Area per polymer volume [µm^2/µm^3]	30.41	19.88	35.04	21.23	37.69	39.35
Number of individual pores	14164	9260	17500	8132	34431	73800

Table 1: Summary of pore volume and surface area measurements as determined via FIB/SEM tomography data. The total sampled volume of each data set was 4.56 µm³. MIP0 and NIP0 were pure DVB-based polymers; MIPH0 and NIPH0 were pure DVB-based polymers hydrolyzed after polymerization; MIPH40 and NIPH40 were polymers comprising a mixture of 60:40 DVB:EGDMA as cross-linker, which were also hydrolyzed after polymerization. Details are given in the experimental section.

Characterization of the pore space

As summarized in Table 1, the total pore volume visualized for all three investigated MIPs is significantly larger than for their non-imprinted counterparts ranging from 0.74 µm³ (MIP0) to 0.61 µm³ (MIPH40) within the sampled volume of 4.56 µm³. The corresponding NIPs range from 0.49 µm³ to 0.43 µm³, and contain approx. 0.2 µm³ less pore volume than the MIPs. In MIPs, the amount of pore space relative to the total sampled volume is approx. 5% higher than in the NIPs. A similar trend is observed for the pore surface area for pure DVB MIP/NIP polymers. For hydrolyzed MIPs/NIPs using DVB/EGDMA mixtures as cross-linker, the total surface area is almost the same, although the total pore volume appears to be different. NIPH40 contains more than twice as much individual, not-connected pore space compared to MIPH40. These are necessarily smaller pores than those within MIPH40, as otherwise the total pore volume should be higher and not smaller. The general trend of NIPs revealing smaller pore sizes compared to MIPs is clearly evident when plotting the pore size distribution, as shown in Fig. 3. Rebinding studies shown in Figure S2 (MIP40 and NIP40) clearly result in higher binding efficiency for MIP in comparison with the NIP.

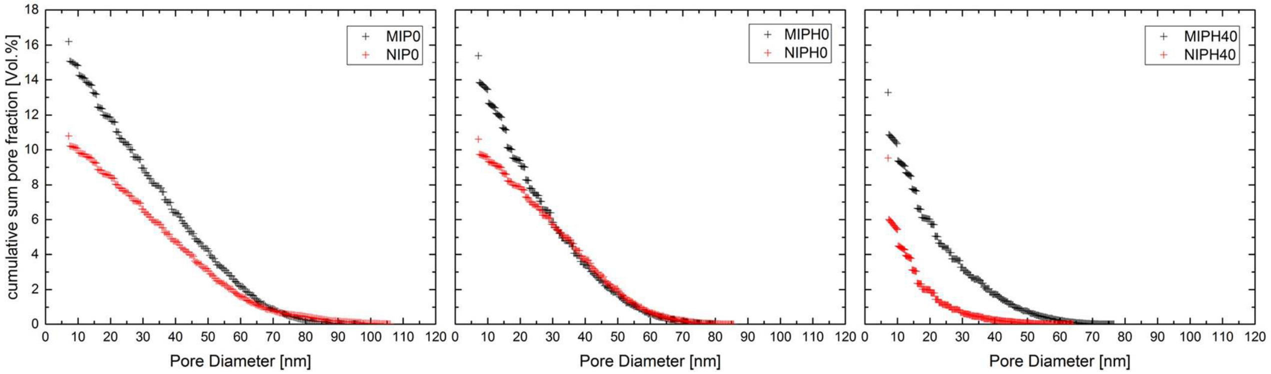

Fig. 3 Pore size distribution obtained by FIB/SEM tomography represented as cumulative pore volume vs. pore diameter. The minimum resolvable diameter in pore size is approx. 7 nm; pores smaller than that may occur in the sampled volume but cannot be resolved in the presented study. A higher total pore volume of the MIPs relative to their non-imprinted counterparts as is clearly evident. Likewise, larger pores are resulting for each investigated MIP/NIP pair. Hydrolyzed MIPs and NIPs containing EGDMA reveal lower total pore volumes, and significant smaller pore sizes compared to MIPs/NIPs containing no EGDMA.

Interconnectivity of pores

In Fig. 4 and 5, the pore space is visualized in a line of sight along the z-axis (see also explanatory videos in the supporting information). Images a) and b) in Fig. 4 and 5, respectively, show completely isolated pores within the sampled volume, which are marked in red. These pores have no connection within the sampled volume. It is clearly evident that in the non-imprinted polymers (Fig. 4b), the number of isolated pores is significant higher in comparison to the imprinted polymer (Fig. 4a), where only a small fraction of the pore space is isolated. It has to be noted that the achievable resolution in the present study was approx. 7 nm due to application of a constrained smoothing filter during 3D image processing.

View Article Online
DOI: 10.1039/C7NR05725C

Hence, only pore spaces > 7nm can be visualized. Large pore volumes created by a local interconnection of pore spaces are highlighted in Fig. 4 and Fig. 5 c) and d), respectively, in different colors. All voxels that share the same color are connected in three dimensions within the sampled volume. Purely DVB-based MIPs are characterized by large pores, which apparently form well-connected pore networks extending across the entire sampled volume (Fig. 4c and 5c). (For individual comparisons see Fig. S3-S5). KOH in the methanol/water mixture applied for hydrolysis should only affect EGDMA-containing polymers. However, it appears that hydrolysis is also influencing the interconnectivity of the pore space. As evident in Fig. 5d, the pores within the hydrolyzed DVP/EGDMA-based MIP (MIPH40) are significantly less interconnected compared to MIP0 and MIPH0. However it appears that the visualized network is still more interconnected than all pore networks within the sampled NIPs (Fig. 4d, see also supporting information). The relative percentage change in pore space between MIPH40 and NIPH0 is approx. 28%. Notably, the pore space within the NIPs is clearly less connected compared to the respective MIPs, which are apparently characterized by distinct pore networks, at least within the sampled volumes. Evidently, MIPs still contain a significant number of isolated pores potentially containing non extracted template molecules, which is consistent with previous findings by Meier et al..[12]

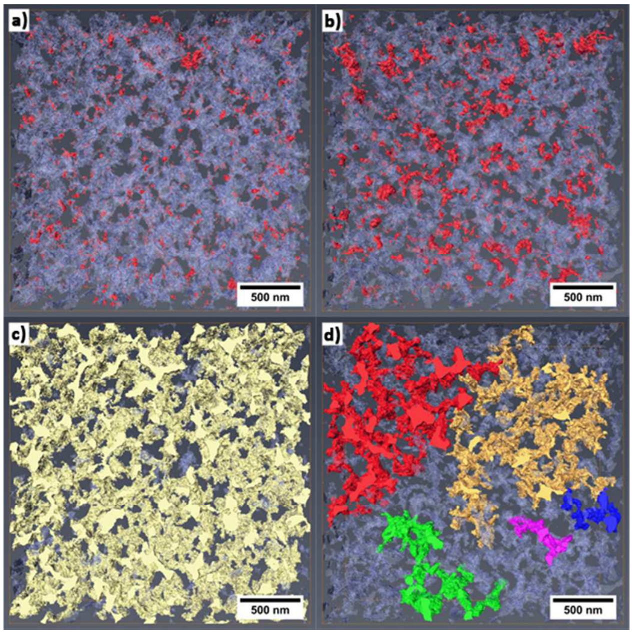

Fig. 4 3D visualization of pore space presented in transparent blue for MIP0 in a) and c), and NIP0 in b) and d). The highlighted pores in red color shown in a) and b) represent pore space, which is isolated within the sampled volume. None of these pores have a connection to the front facet of the sampled volume. In c) and d), large interconnected pore spaces marked with the same color with sections that are connected to each other, and to the front facets. c) shows the MIP network, which is distributed within the entire sampled volume. NIP pore networks marked in d) clearly reveal smaller interconnected areas.

MIP and NIP pairs were synthesized following the same protocol with the only difference that propranolol - the template molecule - was present or absent during the polymerization reaction. As a pre-polymerization complex involving the template molecule is formed during MIP synthesis prior to the actual polymerization, which is not formed in absence of the template molecule (i.e., synthesis of NIPs), polymers with less interconnected pore spaces are resultant.

The template and/or the formation of pre-polymerization complexes appear to affect locally the radical polymerization process. Thus, it is hypothesized that cross-linking within the polymer matrix is affected giving rise to the observed structural differences in porosity of MIP and NIP, respectively.

Although only pore spaces > 7 nm can be visualized by FIB/SEM tomography in the present study, evident differences in pore interconnectivity have readily been shown. Consequently, next to differences observed in MIPs and NIPs during evaluation of their binding resulting from the actual ‘imprinting’ procedure, differences in local porosity and accessible surface area cannot be neglected. Especially, it appears that not only the surface area of the pores, but also their interconnection are important factors affecting the amount of template molecules, which can be bound or adsorbed by the respective polymer matrix. This important aspect should clearly be considered, if MIPs and NIPs are compared in terms of their binding behavior.

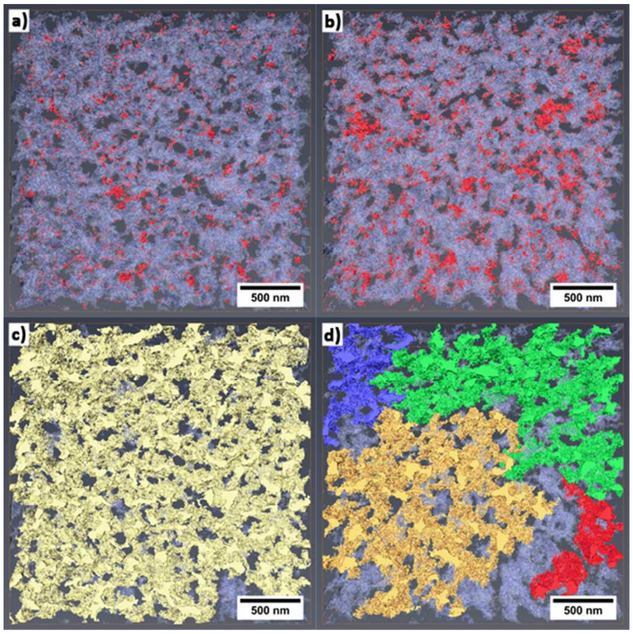

Fig 5. 3D visualization of pore space presented in transparent blue for MIPH0 in a) and c), and MIPH40 in b) and d). The highlighted pores in red color shown in a) and b) show pore space, which is isolated within the sampled volume. None of these pores have a connection to the front facet of the sampled volume. In c) and d), large interconnected pore spaces are marked with the same color with sections that are connected to each other, and to the front facet. MIPH0 pore space marked in c) shows a network, which is distributed among the entire

View Article Online
DOI: 10.1039/C7NR05725C

sampled volume similar to the scenario in Fig. 4 c). The MIPH40 networks marked in d) clearly indicate the change induced by hydrolysis of the polymer.

BET/BJH measurements vs. FIB/SEM tomography

The most commonly applied methods for pore space investigations of MIPs and NIPs are BET and BJH studies. Both methods provide access to the total pore volume and surface area of the samples, which may also be derived via FIB/SEM tomography, as shown herein. However, a direct comparison and correlation of the data achieved by BET/BJH and FIB/SEM tomography is difficult, because BET/BJH data are usually related to mass, whereas tomography data are related to the sampled volume. Hence, for a useful comparison precise knowledge on the density of the polymer material is usually required. Alternatively, the pore space distribution functions may be derived for both data sets, as shown by Keller et al.,[26] thereby facilitating a direct comparison of BET and FIB/SEM tomography data without a priori knowledge on the material density. Within the achievable FIB/SEM resolution, both data sets align well, with the differences attributed to the limited resolution in FIB/SEM tomography. As anticipated, volume and surface are data derived from FIB/SEM tomography underestimates the true pore space, as pores < 7 nm are not considered in contrast to BET/BJH. In turn, BET/BJH measurements may overestimate the pore volume/surface area, as the sample surface is included as well. A notable difference between both methods is the amount of sampled volume. The sample volume addressed in FIB/SEM tomography is comparatively small (herein, approx. 4.56µm³), whereas BET/BJH measurements are derived from significantly larger amounts of material. Hence, while each method has its merits and limitations, only FIB/SEM tomography provides information on the internal structure of a pore network including connectivity, pore space distribution, and even pore orientation in three dimensions, which fundamentally contributes to a detailed understanding of functional materials such as molecularly imprinted polymers at a nanoscale.

Conclusions

To the best of our knowledge, FIB/SEM tomography has not been used to date for investigating the distribution and interconnectivity of pores within molecularly imprinted polymers (MIPs), and their non-imprinted counterparts (NIPs). Staining MIP and NIP polymer particles with OsO_4 vapor provides useful contrasts for high-resolution electron microscopy imaging readily enabling the discrimination between pore space and polymer matrix. Herein, a strategy was developed, which allows investigating the properties of the pore space in detail revealing and visualizing significant pore interconnectivity differences between MIPs and NIPs. Furthermore, FIB/SEM tomography provides information on the pore surface and pore volume only limited by the achievable spatial resolution. Comparing FIB/SEM tomography data to BET/BJH measurements revealed a reasonable coincidence of the data sets. Finally, it was demonstrated that FIB/SEM tomography allows pinpointing the influence of chemical parameters on the finally obtained pore properties including the selection of cross-linker, and the influence of chemical treatment such as hydrolysis. Summarizing, an alternative method is presented for the characterization of the pore distribution, interconnectivity, and tortuosity enabling visualization of differences between imprinted and non-imprinted polymers. Typically, only the absence of specific binding sites is considered relevant for differences in binding behavior between MIP and NIP. The present study clearly demonstrates that significant differences in pore structure and pore properties at the nanoscale may be of significant additional influence. The presented study is not limited to bulk polymerized polymers and will be used for spherical MIP particles in the future.

Acknowledgements

Financial support by the German BMBF within projects PROTSCAV I & II is greatly appreciated. The authors also acknowledge the Focused Ion Beam Center UUlm for enabling FIB/SEM tomography. E. Schmid at the Central Electron Microscopy Facility UUlm is acknowledged for assistance in embedding and staining of the polymer samples.

Experimental

MIP synthesis

Propranolol MIPs were synthesized using a bulk preparation protocol. Propranolol hydrochloride (Sigma) was converted to the free base by titration of an aqueous solution with concentrated sodium hydroxide solution. The precipitate was collected and dried. The propranolol free base was then dissolved in acetonitrile (Fisher Chemicals) and toluene (Acros Organics). Methacrylic acid (Sigma) as functional monomer, different ratios of divinylbenzene (DVB) (Aldrich) and ethylene glycol dimethacrylate (EGDMA) (Aldrich) were used as cross-linkers (MIP0: 100% DVB; MIP40: 60% DVB, 40% EGDMA) and 1,1'-Azobis(cyclohexanecarbonitrile) (ABCN) (Aldrich) as radical initiator were added. The mixture was degassed with nitrogen for 4 minutes and polymerized for 18 h at 95°C. After polymerization, the monolith was crushed and sieved, and the fraction with particle sizes of 25-63 µm was separated for analysis. The template was removed by excessively washing the polymer fraction with 90% methanol (Fisher Chemicals) and 10% acetic acid (Fisher Chemicals), and finally with pure methanol in tubes under gentle rocking. The particles were then dried in a vacuum oven (Gallenkamp) at 40°C prior to usage. The non-imprinted (NIP) particles were prepared in the same way without adding propranolol-free base to the reaction mixture. 400 mg fractions of the synthesized polymers were hydrolyzed by adding 20 mL of a 3.66 M KOH solution (MeOH / H2O; 2:1 (v/v)) and heating to 60°C over night in sealed vials. The particles were then washed with 50%

View Article Online
DOI: 10.1039/C7NR05725C

methanol 50% water followed by 80% methanol 20% acetic acid, and finally, by pure methanol.

Sample preparation and FIB/SEM tomography procedure

Small portions of the MIP and NIP particles were placed overnight in a sealed container together with an osmium tetroxide crystal. Osmium tetroxide is highly volatile and forms an OsO_4-enriched vapor, which “stains” the polymer matrix of the MIP and NIP, respectively by reacting with double bonds of the sample[36] Such a treatment enriches osmium (Os) within the polymer network and therefore enhances the contrast achievable in the recorded SE images (Fig.1 c).[38] After the modification with Os, all samples were embedded in Epon epoxy (Sigma Aldrich) using small Eppendorf vials by polymerization at 60 °C within 72 h. The resulting Epon blocks were cut using a diamond knife to obtain a sample of approx. 1x1 cm width and a thickness of 1mm with a flat, smooth surface. After cutting, the samples were sputtered with an approx. 3-4 nm thick platinum layer to reduce eventual charging effects during FIB/SEM.

Swelling studies were performed with MIP0 and NIP0 polymer particles using a Zeiss Axio Scan.Z1 microscope. The surface area of the same grains prior and after embedding were marked and measured using Fiji software package[39].

FIB/SEM tomography was performed using a Helios Nanolab 600 (FEI Company, NL). First, an approximately 700 nm thick additional platinum protection layer was deposited via ion beam induced deposition (IBID) with methylcyclopentadienyl trimethyl platinum ($C_9H_{16}Pt$) as precursor. The sample surface was modified in two steps, first for 5 min deposition was performed with 30kV and 48pA to avoid sputtering of the sample surface, then the current was raised to 0.28 nA to accelerate the deposition process. The two-step deposition process avoids the formation of holes just beneath the protection layer at the sample surface. These holes dramatically increase the probability of curtaining artifacts during the milling process. In a next step, a wedge was excavated at 30 kV and 9.3 nA. The front perpendicular facet towards the surface was cleaned from residual and amorphous material using stepwise smaller beam currents down to 0.28 nA.

FIB/SEM Tomography was performed using the ‘slice-and-view’ software package (FEI Company) (as schematically shown in Fig 1a). Automated serial milling was obtained at 30 kV and 48 pA and secondary electron (SE) image were acquired at 5kV and 86 pA using the immersion mode and the through the lens detector (TLD) of the microscope. A volume of 2.5 x 2.5 x 0.73 µm was investigated in each sample with a resolution of 3.57 x 3.57 x 5 nm (voxel size).

Data processing

All image stacks were processed the same way using the free software package Fiji.[39] The first step was the alignment of all images within a stack using the plugin “Linear Stack Alignment with SIFT” with an expected transformation of a translation avoiding turning of the images during the alignment process.[40] After alignment, a FFT bandpass filter was applied to all stacks for correction of differences in the image brightness (shadowing effects) and to enhance contrast in all images. In a third step, all image stacks were binarized by a certain threshold. The grey value for the threshold was set half of the grey value of the peak in the stack histogram (see Fig 2c). Quantitative data concerning volume and surface area of the pore space was obtained using the “3D object counter” plugin included in Fiji to the processed image stacks.[41] Pore space distribution data was achieved by using the “local thickness (masked, calibrated, silent)” plugin programmed by Bob Dougherty[42] on each binarized image stack. 3D visualization of the image stacks was done with Avizo 9.1.0 Lite (FEI Company). The isolated pore space shown in Fig. 4 and 5 was achieved by removing all pixels that have a connection to the lateral faces of the sampled volume. Visualization of connecting pores as shown in Fig. 4 & 5 was achieved by highlighting an individual pore at the front face of the sampled volume and all black pixels connected to that marked area in 3D.

View Article Online
DOI: 10.1039/C7NR05725C

References

1. Z. Chen, X. Wang, F. Giuliani, and A. Atkinson, *J. Power Sources*, 2015, **273**, 486–494.
2. Z. Liu, Y. K. Chen-Wiegart, J. Wang, S. A. Barnett, and K. T. Faber, *Microsc. Microanal.*, 2017, **22**, 140–148.
3. D. Moore, X. He, A. Ben Azouz, E. Nesterenko, P. Nesterenko, B. Paull, and D. Brabazon, *Analyst*, 2014, **139**, 99–104.
4. S. S. Ray, *Polymer*, 2010, **51**, 3966–3970.
5. M. Cieplak and W. Kutner, *Trends Biotechnol.*, 2016, **34**, 922–941.
6. J. L. Bowen, P. Manesiotis, and C. J. Allender, *Mol. Imprinting*, 2013, **1**, 35–40.
7. G. Cirillo, F. Iemma, F. Puoci, O. I. Parisi, M. Curcio, U. G. Spizzirri, and N. Picci, *J. Drug Target.*, 2009, **17**, 72–77.
8. J. Wackerlig and R. Schirhagl, *Anal. Chem.*, 2016, **88**, 250–261.
9. P. Zahedi, M. Ziaee, M. Abdouss, A. Farazin, and B. Mizaikoff, *Polym. Adv. Technol.*, 2016, **27**, 1124–1142.
10. H. S. Andersson and I. A. Nicholls, *Bioorg. Chem.*, 1997, **25**, 203–211.
11. J. O'Mahony, S. Wei, A. Molinelli, and B. Mizaikoff, *Anal. Chem.*, 2006, **78**, 6187–6190.
12. F. Meier, S. M. Elbert, and B. Mizaikoff, *Anal. Methods*, 2012, **4**, 2296–2299.
13. M. Ulbricht, *Polymer*, 2006, **47**, 2217–2262.
14. U. G. Spizzirri, N. A. Peppas, V. Uni, U. V Station, R. V December, V. Re, M. Recei, and V. October, *Chem. Mater.*, 2005, **17**, 6719–6727.
15. S. Brunauer, P. H. Emmett, and E. Teller, *J. Am. Chem. Soc.*, 1938, **60**, 309–319.
16. E. P. Barrett, L. G. Joyner, and P. P. Halenda, *J. Am. Chem. Soc.*, 1951, **73**, 373–380.
17. H. Giesche, *Part. Part. Syst. Charact.*, 2006, **23**, 1–11.
18. J. L. Urraca, M. C. Carbajo, M. J. Torralvo, J. González-Vázquez, G. Orellana, and M. C. Moreno-Bondi, *Biosens. Bioelectron.*, 2008, **24**, 155–161.
19. A. Ben Aissa, A. Herrera-Chacon, R. R. Pupin, M. D. P. T. Sotomayor, and M. I. Pividori, *Biosens. Bioelectron.*, 2017, **88**, 101–108.
20. M. . Kral, M. . Mangan, G. Spanos, and R. . Rosenberg, *Mater. Charact.*, 2000, **45**, 17–23.
21. C. Villinger, H. Gregorius, C. Kranz, K. Höhn, C. Münzberg, G. von Wichert, B. Mizaikoff, G. Wanner, and P. Walther, *Histochem. Cell Biol.*, 2012, **138**, 549–556.
22. F. Schmidt, M. Kühbacher, U. Gross, A. Kyriakopoulos, H. Schubert, and R. Zehbe, *Ultramicroscopy*, 2011, **111**, 259–266.
23. L. Holzer, F. Indutnyi, P. H. Gasser, B. Münch, and M. Wegmann, *J. Microsc.*, 2004, **216**, 84–95.
24. G. Spanos, D. J. Rowenhorst, A. C. Lewis, and A. B. Geltmacher, *MRS Bull.*, 2008, **33**, 597–602.
25. N. Norberg, G. Neusser, R. Wirth, and D. Harlov, *Contrib. to Mineral. Petrol.*, 2011, **162**, 531–546.
26. L. M. Keller, L. Holzer, R. Wepf, and P. Gasser, *Appl. Clay Sci.*, 2011, **52**, 85–95.
27. C. Villinger, G. Neusser, C. Kranz, P. Walther, and T. Mertens, *Viruses*, 2015, **7**, 5686–5704.
28. P. Walther and A. Ziegler, *J. Microsc.*, 2002, **208**, 3–10.
29. A. Sheidaei, M. Baniassadi, M. Banu, P. Askeland, M. Pahlavanpour, N. Kuuttila, F. Pourboghrat, L. T. Drzal, and H. Garmestani, *Compos. Sci. Technol.*, 2013, **80**, 47–54.
30. K. Booker, C. I. Holdsworth, C. M. Doherty, A. J. Hill, M. C. Bowyer, and A. McCluskey, *Org. Biomol. Chem.*, 2014, **12**, 7201–7210.
31. I. Iturralde, M. Paulis, and J. R. Leiza, *Eur. Polym. J.*, 2014, **53**, 282–291.
32. Z. Adali-Kaya, B. T. S. Bui, A. Falcimaigne-Cordin, and K. Haupt, *Angew. Chemie, Int. Ed.*, 2015, **54**, 5192–5195.
33. V. P. Joshi, M. G. Kulkarni, and R. A. Mashelkar, *J. Chromatogr. A*, 1999, **849**, 319–330.
34. N. Holland, J. Frisby, E. Owens, H. Hughes, P. Duggan, and P. McLoughlin, *Polymer*, 2010, **51**, 1578–1584.
35. R. Vendamme, W. Eevers, M. Kaneto, and Y. Minamizaki, *Polym. J.*, 2009, **41**, 1055–1066.
36. M. A. Parker and D. Vesely, *Microsc. Res. Tech.*, 1993, **24**, 333–339.
37. E. A. Wargo, T. Kotaka, Y. Tabuchi, and E. C. Kumbur, *J. Power Sources*, 2013, **241**, 608–618.
38. G. H. Michler, in *Electron Microscopy of Polymers*, Springer-Verlag, Berlin Heidelberg, 1st Editio., 2008, pp. 241–260.
39. J. Schindelin, I. Arganda-Carreras, E. Frise, V. Kaynig, M. Longair, T. Pietzsch, S. Preibisch, C. Rueden, S. Saalfeld, B. Schmid, J.-Y. Tinevez, D. J. White, V. Hartenstein, K. Eliceiri, P. Tomancak, and A. Cardona, *Nat. Methods*, 2012, **9**, 676–682.
40. D. G. Lowe, *Int. J. Comput. Vis.*, 2004, **60**, 91–110.
41. S. Bolte and F. P. Cordelières, *J. Microsc.*, 2006, **224**, 213–232.
42. https://imagej.net/Local_Thickness

Electronic Supplementary Material (ESI) for Nanoscale.

SUPPORTING INFORMATION

FIB and MIP: Understanding Nanoscale Porosity in Molecularly Imprinted Polymers via 3D FIB/SEM Tomography

G. Neusser, S. Eppler, J. Bowen, C. J. Allender, P. Walther, B. Mizaikoff,* and C. Kranz*

	Template Propranolol	**Functional monomer** Methacrylic acid (MAA)	**Cross linker** Divinylbenzene (DVB)	**Crosslinker** Ethylene glycol dimethacrylate (EGDMA)	**Hydrolyzation** Potassium hydroxide (KOH)
MIP0	Yes (1.61 mmol)	Yes (6.44 mmol)	100% (30.93 mmol)	0% (-)	no
MIPH0	Yes (1.61 mmol)	Yes (6.44 mmol)	100% (30.93 mmol)	0% (-)	yes
MIPH40	Yes (1.61 mmol)	Yes (6.44 mmol)	60% (18.56 mmol)	40% (12.37 mmol)	yes
NIP0	no	Yes (6.44 mmol)	100% (30.93 mmol)	0% (-)	no
NIPH0	no	Yes (6.44 mmol)	100% (30.93 mmol)	0% (-)	yes
NIPH40	no	Yes (6.44 mmol)	60% (18.56 mmol)	40% (12.37 mmol)	yes

Table 1: Composition of investigated molecularly imprinted polymers (MIPs) imprinted for propranolol

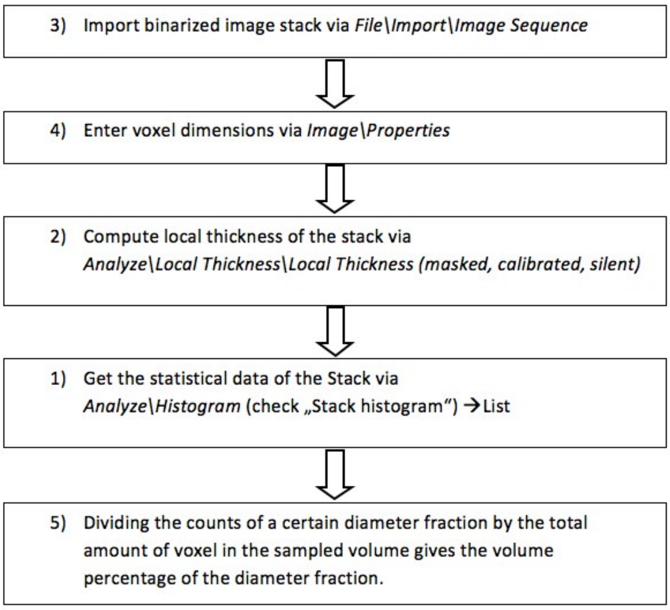

3) Import binarized image stack via *File\Import\Image Sequence*

4) Enter voxel dimensions via *Image\Properties*

2) Compute local thickness of the stack via *Analyze\Local Thickness\Local Thickness (masked, calibrated, silent)*

1) Get the statistical data of the Stack via *Analyze\Histogram* (check „Stack histogram") → List

5) Dividing the counts of a certain diameter fraction by the total amount of voxel in the sampled volume gives the volume percentage of the diameter fraction.

Figure S1: Flow chart for evaluating the pore space distribution using FIB/SEM tomography

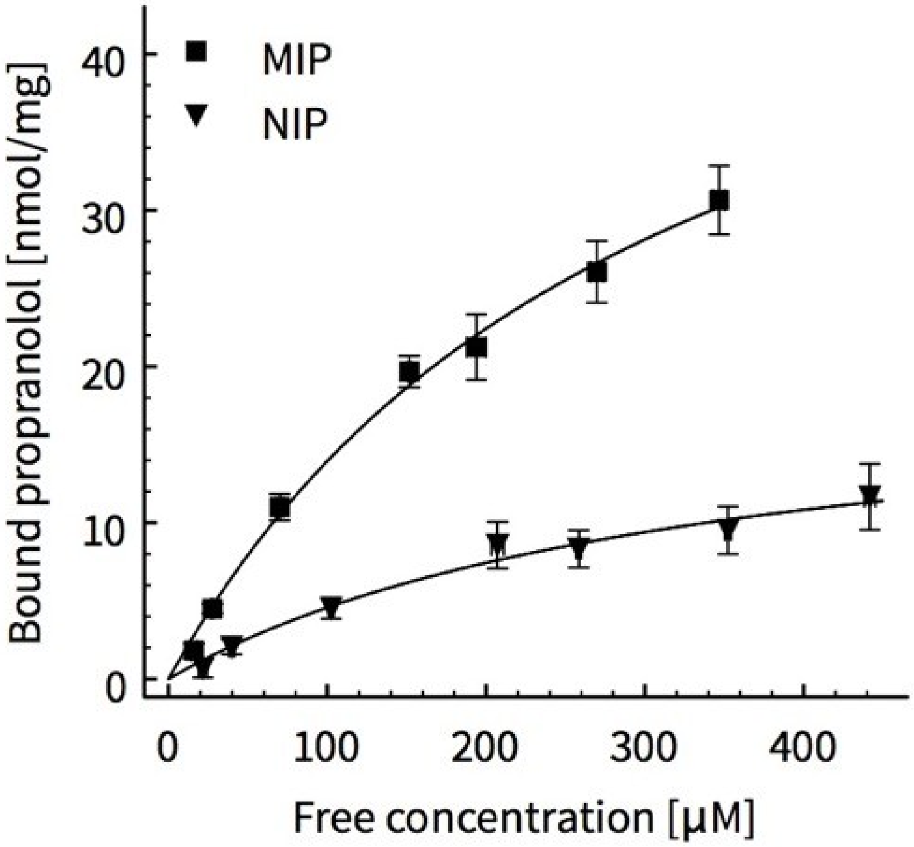

Figure S2: Exemplary rebinding curve for MIP40 and NIP40 using filter plate incubation. Data were obtained using a conventional UV well plate reader at 290 nm (N = 3). Isotherms fitted using Prism 5 software and the implemented analyzing tool with "one site – specific binding" (equates Langmuir isotherm) model.

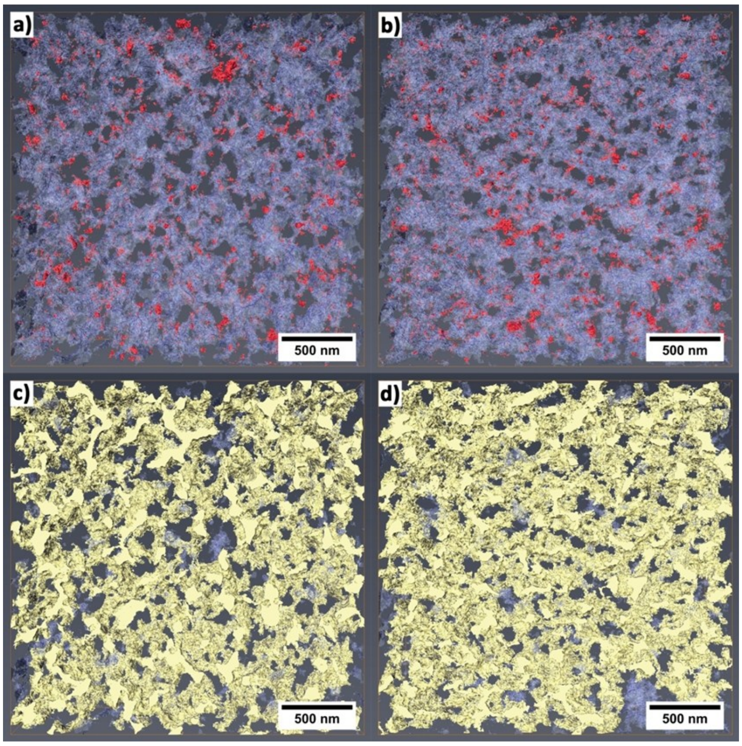

Figure S3: 3D visualization of pore space presented in transparent blue for MIP0 in a) and c), and MIPH0 in b) and d). The highlighted pores in red color presented in a) and b) show pore space, which is isolated within the sampled volume. None of these pores have a connection to the front facet of the sampled volume. In c) and d), large interconnected pore spaces are marked with the same color with sections that are connected to each other, and to the front facet. MIP0 pore space marked in c) shows a network, which is distributed among the entire sampled volume as do the MIPH0 networks marked in d). There is no significant difference between both pore networks visible in terms of interconnectivity.

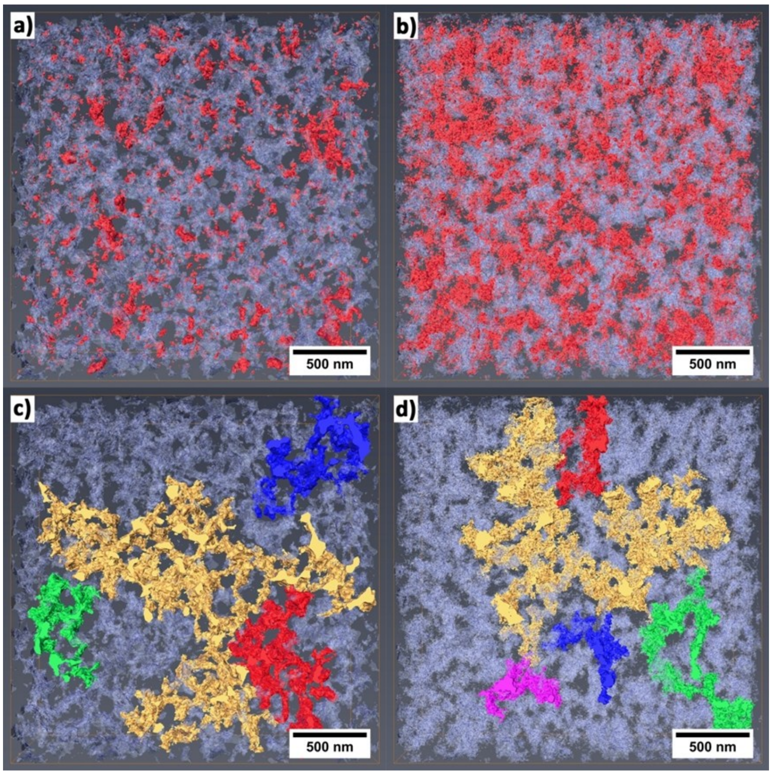

Figure S4: 3D visualization of pore space presented in transparent blue for NIPH0 in a) and c), and NIPH40 in b) and d). The highlighted pores in red color presented in a) and b) show pore space, which is isolated within the sampled volume. None of these pores have a connection to the front facet of the sampled volume. In c) and d), large interconnected pore spaces are marked with the same color with sections that are connected to each other, and to the front facet. NIPH40 shows much more isolated pore space than NIPH0.

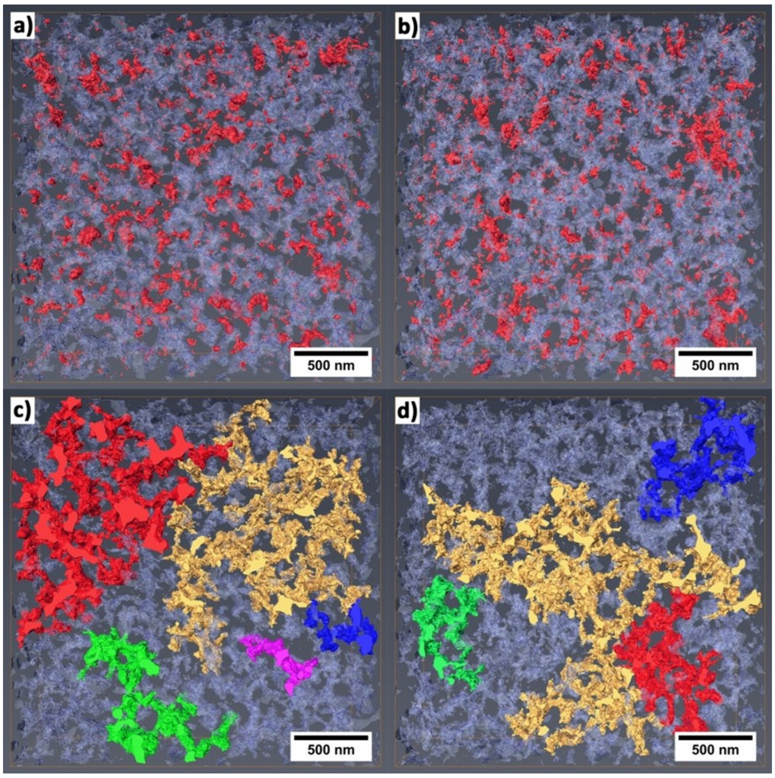

Figure S5: 3D visualization of pore space presented in transparent blue for NIP0 in a) and c), and NIPH0 in b) and d). The highlighted pores in red color presented in a) and b) show pore space, which is isolated within the sampled volume. None of these pores have a connection to the front facet of the sampled volume. In c) and d), large interconnected pore spaces are marked with the same color with sections that are connected to each other, and to the front facet. As for their MIP counter parts NIP0 and NIPH0 show no significant difference in pore space connectivity.